C$_{60}$ adsorption on the Si(111)-p(7×7) surface: A theoretical study

R. Rurali

Departament d'Enginyeria Electrònica, Universitat Autònoma de Barcelona, 08193 Bellaterra, Spain
and Institut de Ciència de Materials de Barcelona, ICMAB-CSIC, Campus de Bellaterra, 08193 Bellaterra, Barcelona, Spain

R. Cuadrado and J. I. Cerdá

Instituto de Ciencia de Materiales de Madrid CSIC, Cantoblanco, 28049 Madrid, Spain

We present density-functional theory calculations of the adsorption of C$_{60}$ on the Si(111)-p(7×7) surface. We have considered seven different adsorption configurations, including the corner hole and other adsorption sites with a high degree of coordination with the dangling bonds of the surface. Tight-binding molecular dynamics suggest that the highly reactive adatoms and rest atoms of the (7×7) reconstruction are always able to adjust the C$_{60}$ position—rotating it and displacing it—so that one of such adsorption configurations is possible. We have then performed scanning tunneling microscopy and scanning tunneling spectroscopy simulations of the adsorbed geometries, taking explicitly into account the tip, i.e., beyond the Tersoff-Hamann approach, and considering both a Pt and a W tip structure.

I. INTRODUCTION

The interface between organic molecules and surfaces has attracted great interest in recent years due to their potential use in molecular electronics,[1] information technology,[2] or biomedical[3] applications. Among candidate molecules C$_{60}$ stands out for its interesting properties ranging from the formation of ordered self-assembled nanostructure on some substrates[4] to the possibility of targeted drug delivery which has recently been explored.[3] Considerable experimental and theoretical efforts have been devoted to the study of the physics of the adsorption of C$_{60}$ on silicon,[5–13] and much progress on its manipulation have been reported[14–18] as well. The characterization of this system is particularly challenging due to the plethora of metastable adsorption geometries available as a consequence of both the large size of the C$_{60}$ and the multiple *active* dangling bonds present at the surface. Depending on the orientation of the molecule and the number of covalent bonds it forms with the silicon atoms, the fullerenes may either physisorb or chemisorb covering a wide range of adsorption energies.

On Si(100) Hobbs *et al.* calculated a wealth of adsorption configurations for the C$_{60}$,[8] the most stable ones forming three to four covalent bonds to the surface. Furthermore, scanning tunneling spectroscopy (STS) spectra have been found to be very sensitive to the precise adsorption geometry[6,7] at the surface. The other widely studied Si surface is the Si(111)-p(7×7) reconstruction for which the landscape of metastable C$_{60}$ adsorption geometries is even larger. In an STM study Hou *et al.*[13] identified four possible fullerene adsorption sites on the (7×7) surface, namely, corner hole (CH), faulted and unfaulted halves (FH and UH), and dimer lines. For the three former cases they were able to image intramolecular features which showed a strong dependence with the bias polarity. At positive voltages, a sort of tilted pentagon surrounded by three elongated bumps could be resolved, although the tilt angle from the surface normal varied depending on the adsorption site. At negative biases,

on the other hand, four roughly parallel stripes were imaged. Similar internal features for the fullerenes adsorbed at the FH, UH, and CH have been recently reported by Huang *et al.* in a room-temperature scanning tunneling microscopy (RT-STM) study.[11] STS measurements for these configurations were found to be site dependent,[9] although in all cases the spectra revealed a strong hybridization between the C$_{60}$ molecular orbitals (MOs) and the surface states, with certain charge transfer from the latter to the fullerene. In another STM experiment Pascual *et al.* imaged the fullerenes with two clearly different apparent sizes;[10] the larger ones were less stable and after annealing they converted into the more stable smaller ones. Different internal structures were found for the small molecules depending on bias, tip conditions or the precise adsorption site, although they all share certain similarities with the above mentioned works.

From the theoretical side, most studies have relied on density-functional theory (DFT) but have employed several approximations due to the large (7×7) supercell size. Hou *et al.* and Wang *et al.* used a cluster approach but did not take into account any fullerene's or Si surface restructuring upon adsorption[9,13] but only optimized the C$_{60}$ height assuming two different orientations. Still, the calculations led to Tersoff-Hamann images which reproduced the intramolecular structures at both the CH and the F/UHs (Ref. 13) for positive and negative biases and for specific C$_{60}$ orientations. At positive biases—empty states—the internal features could be directly assigned to the unoccupied MOs of the isolated fullerene, whereas at negative biases—occupied states—there was a strong discrepancy in the aspect between the isolated and adsorbed molecule. Moreover, the density of states projected on the C$_{60}$ MOs for the CH case was in good agreement with its measured STS spectra.[9] Pascual *et al.*, on the other hand, associated the different types of images to the fullerene's highest occupied molecular orbital (HOMO) after applying a slight distortion to the isolated molecule and comparing the associated local density of states (LDOS) against the experimental internal features. The F/UH adsorption ge-

ometries have been later revisited adopting a reduced $(2\sqrt{3} \times 2\sqrt{3})R30°$ supercell, this time fully relaxing the entire system. The relaxations were indeed found to be very large and essential to the stability of the adsorbed C_{60}, while several metastable phases could be identified depending on the initial molecule's orientation and adsorption site in the total-energy minimizations.[12,19] Surprisingly, the Tersoff-Hamann (TH) images at negative biases for these new optimized geometries hardly fitted the experimental images, in contrast with the simulations of Hou *et al.* despite their guessed geometry is less reliable.

In summary, the STM experimental works agree in the multiple C_{60} chemisorbed sites, FH, UH, and CH while the detailed intramolecular features at each of these sites are not unique but show certain differences between the different experiments. The interpretation of these internal features is, however, contradictory.

In this work we perform a thorough survey of the precise adsorption geometries covering the entire Si(111)-p(7×7) supercell, which is still lacking from the theoretical point of view. To this end, we combine tight-binding molecular-dynamics (TB-MD) calculations with DFT based total-energy calculations. We analyze in detail up to seven different configurations including the simulation of their respective STM images and STS. In Sec. II we will summarize our approach to both the determination of the different adsorption geometries and the simulations of STM images and STS spectra. Our results will be presented and discussed in Sec. III, leaving the last section for a summary of the conclusions of the paper.

II. THEORY

We have performed DFT calculations with the SIESTA package[20] using norm-conserving pseudopotentials for the core electrons and the local-density approximation (LDA) for the exchange-correlation energy. The one-electron wave function has been represented with a double-ζ polarized basis set,[21] optimized following Anglada *et al.*[22] We have used one unit cell of the (7×7) reconstruction of the Si(111) surface in slab geometry. The slab was made of two bilayers plus the required surface adatoms to describe the (7×7) reconstruction. The bottom bilayer, whose dangling bonds were terminated with hydrogens, was kept frozen, while the remaining atoms were relaxed until the maximum force was smaller than 0.04 eV/Å. Because of the large size of the simulation cell the Brillouin zone was sampled with the Γ point only.

As we discuss in Sec. III A 1 we have also performed a limited series of molecular-dynamics simulation in the microcanonical ensemble to gain some qualitative hints on the favored sites for the adsorption of the fullerene. For these simulations the total energy and the forces were calculated within the computationally lighter tight-binding scheme of Porezag *et al.*[23] as implemented in the TROCADERO package.[24]

The results of the STM/STS simulations presented in Sec. III B have been calculated with the GREEN code.[25,26] Tip and sample are modeled at the atomic level as two semi-infinite
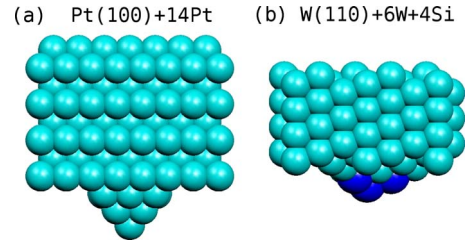

FIG. 1. (Color online) Side views of the two tip models employed in the STM/STS simulations. (a) A semi-infinite Pt(100) bulk block with a 14 Pt atoms cluster. (b) A semi-infinite W(110) bulk block with six W plus four Si atoms (blue) cluster.

bulklike blocks. The sample is a (111)-oriented Si bulk on top of which the reconstructed (7×7) surface plus the C_{60} molecule are stacked following the DFT derived geometry. The tip consists of a metallic bulk terminated by an isolated apex cluster with a pyramidal shape comprising a few atoms. Again, the apex geometry is obtained from DFT calculations. We have considered two different tips depicted in Fig. 1. First, a sharp one-atom ended Pt(100) oriented metallic tip [Fig. 1(a)] and, second, a more blunt W(110) oriented tip ended with a rectangular pyramid made of 6 W atoms at its base and 4 Si atoms at the apex [Fig. 1(b)]. The latter was considered in order to address the possible transfer of Si atoms from surface to tip during the scanning process.[27]

The STM setup is modeled by bringing the tip and sample blocks close to each other ensuring that the surface-apex distance, d_{sa}, corresponds to the tunneling regime, i.e., $d_{sa} > 4$ Å. The elastic current flowing from one lead to another is then evaluated via Green's function techniques following the formalism described in Refs. 25 and 26. Given the complexity of the combined tip-sample STM system, we replace the self-consistent Hamiltonian employed for the energy optimizations by the simpler extended Hückel theory (EHT).[28] The EHT related parameters are optimized separately for the tip and the surface after fitting the atom projected Density of States (PDOS) to those obtained from the *ab initio* calculations.[28,29] More specifically, we first obtained EHT parameters for C in the isolated fullerene varying the on-site energies and the Slater exponents and coefficients. The parameters were then transferred to the fullerene-surface system where due to the large computational cost of the fits, only the C and Si on-site energies were further refined for each adsorption model. Examples of such fits are given in Sec. III A 2.

The STM system Green's function is then evaluated at the EHT level and up to first order in the surface-apex interactions. The potential drop, V, is assumed to be confined in the vacuum region; i.e., apex and surface are in equilibrium with the tip and sample bulk blocks, respectively. This last assumption is known to fail at semiconductor surfaces where the limited electron transport drives any surface state bands out of equilibrium with respect to the bulk thus yielding STS spectra with peaks shifted from their equilibrium energy values.[30] However, on the Si(111)-p(7×7) surface the surface conductivity is thermally activated at room temperature and the RT-STS experiments provide a *true* energy scale.[30] Our approach, therefore, is only applicable here within the

RT regime. The expression for the tunneling current at each relative surface-apex position, $\vec{r}_{sa}$, and for an applied bias V, is given by[26]

$$I(V, \vec{r}_{sa}) = \frac{2e}{h} \int_{-\infty}^{\infty} T(E, V, \vec{r}_{sa})[f_{FD}(E - \mu_s) - f_{FD}(E - \mu_a)]dE$$

$$(1)$$

where f_{FD} gives the Fermi-Dirac distribution function at each electrode and $T(E, V, \vec{r}_{sa})$ corresponds to the transmission function giving the probability that an electron of energy E will leave the first contact and will reach the second reservoir contact. Within GREEN, $T(E, V, \vec{r}_{sa})$ is evaluated according to[26]

$$T(E, V, \vec{r}_{sa}) = \sum_{m_s, m_a} |\langle u_{g_s^0}^m | F_{sa}(\vec{r}_{sa}) | u_{g_a^0}^m \rangle|^2 \qquad (2)$$

where $g_{s/a}^0$ are the so-called contact matrices describing the electronic propagation at the surface and apex and the summation $m_{s/a}$ is restricted to those eigenvectors $|u_{g_{s/a}^0}^m\rangle$ of the contact matrices with nonzero eigenvalues. At each energy E, the contact matrices at the apex are shifted in energy by V with respect to those at the surface. $F_{sa}(\vec{r}_{sa})$ is the secular matrix for the surface-apex interactions. The elements of the eigenvectors $|u_{g_s^0}^m\rangle$ corresponding to the C$_{60}$ atomic orbitals may be trivially transformed to the isolated C$_{60}$ MO basis set, and by retaining the contribution of each MO to $T(E, V, \vec{r}_{sa})$ one can decompose the tunneling current at each $\vec{r}_{sa}$ in terms of the molecules MOs. As will be shown below, this procedure allows us to determine which MOs are the most relevant in the imaging process.

All simulations presented in this work have been computed employing a finite imaginary part of the energy fixed to E_i=50 meV while the energy step employed in the numerical integration of Eq. (1) was set to 25 meV. Test calculations with larger (smaller) E_i values hardly produced any changes in the topographic images and yielded broader (sharper) peaks in the STS spectra without altering their energy locations. The two-dimensional periodicity of the surface and tip blocks was taken into account via Brillouin zone integrations over fine k-space grids; the apex, however, is assumed isolated.[25] Topographic images are obtained by discretizing the (7×7) surface unit cell into a grid of pixels with a lateral resolution of 0.5 Å, i.e., around 3000 pixels per image. At each pixel we varied the surface-apex normal distance, d_{sa}, until the tunneling current attained a preselected value (we always used a set point current of 1 nA). This iterative procedure allows us to extract a numerical estimate for the dI/dz derivative at each pixel as well.

For the STS simulations, we fix the tip height at each pixel to that obtained from the topography and sweep the bias V between −2 and +2 eV. Furthermore, and in order to eliminate the tip convolution from the STS spectra, we freeze the tip electronic structure so that at any energy and bias in the $T(E, V, \vec{r}_{sa})$ calculation we always employ the tips contact matrices evaluated at the Fermi level, $g_a^0(\mu_a)$. This

way, the tip-energy-dependent terms may be pulled out from the energy integral in 1, and the conductance at each pixel becomes

$$dI(V, \vec{r}_{sa})/dV \propto T(E = V, V, \vec{r}_{sa}). \qquad (3)$$

Following the usual experimental convention we will plot $(dI/dV)/(I/V)$ spectra in order to resolve any DOS related peaks. We note that this electronically *frozen* tip approximation is best suited for STS simulations, since the calculated spectra will only display peaks associated to the substrate. On the other hand, for topographic images there is no need to deconvolute the tip contribution since the particular electronic structure of the tip within a given bias will in general affect similarly all pixels in the image.

III. RESULTS AND DISCUSSION

A. Atomic and electronic structure

1. Tight-binding molecular dynamics

In order to simplify the search for minima in such a complex phase space, before performing a systematic study of different adsorption configurations, we have carried out a few MD simulations within the tight-binding scheme. These unbiased MDs, where the adsorption conditions are selected randomly, reduce considerably the probability to miss some deep minimum as a consequence of an unfavorable initial guess. Furthermore, it gives some valuable, though qualitative, information on the dynamics of the adsorption process.

We have *dropped* a C$_{60}$ molecule on the Si(111)7×7 surface giving it an initial velocity of 2.65 10^{-2} Å/fs from approximately 7 Å above the substrate. The in-plane coordinates and the initial orientation of the fullerene have been randomly chosen. Although the computational load of the tight-binding calculations is significantly lower than for the DFT calculations presented in Sec. III A 2, it is still too demanding to perform a massive run of a statistically significant number of samples. Nonetheless, we could obtain some qualitative interesting information.

(a) The tight-binding MDs have sampled configurations that have later turned out to be among the most stable within the systematic series of DFT structural relaxations discussed below, with the only notable exception being the corner hole. This fact confirms the reliability of the tight-binding scheme employed and indicates that there should not be any deep minimum besides the stable configurations that we discuss in Sec. III A 2 (b) The thermal motion of the surface dangling bonds is capable of selecting the best orientation of the C$_{60}$ for its adsorption, translating [Figs. 2(a) and 2(b)] and/or rotating [Figs. 2(c) and 2(d)] it until it can be more tightly bonded. (c) Seldom, the incoming orientation of the C$_{60}$ and the surface site can be particularly unfavorable for the adsorption and the thermal activated atoms at the surface can *backscatter* the fullerene which *rebounds* [Figs. 2(e) and 2(f)]. Remarkably, part of the thermal motion of the surface atoms is transferred to the rigidly incoming C$_{60}$ which, after being backscattered, is left in a vibrationally excited state.
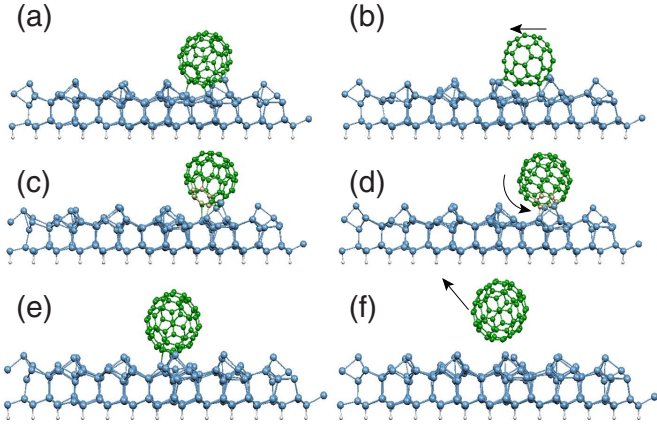
FIG. 2. (Color online) The adatoms adjust the incoming C_{60} until the best conditions for adsorption are satisfied. (a) and (b) the C_{60} is displaced to the left, maximizing its interaction with the highly reactive dangling bonds of the atoms, and ends up in a C_U adsorbed configuration; (c) and (d) the C_{60} is rotated until a hexagon (whose atoms are highlighted with golden spheres) faces down and the molecule binds in a R_U configuration; and (e) and (f) the C_{60} is rebounded and left in a vibrationally excited state.

2. DFT structural relaxations

Based on the adsorbed configurations selected by the tight-binding molecular dynamics and on symmetry considerations we have selected three different initial positions (labeled C, M, and R), each one of which has been calculated in the faulted as well as in the unfaulted half of the (7×7) surface. The positions are shown in Fig. 3. In all the cases the fullerene is at the center of a triangle defined by three adatoms, but at position C and R it *rests* on a rest atom. We label these sites with a subscript F or U, depending on the surface half where they are located; thus, $C_F(C_U)$ indicates a C site at the faulted (unfaulted) half of the (7×7) reconstruction. Besides these six adsorption sites, we have also considered the CH [see Fig. 3(b)]. Our set of initial configurations for the DFT optimizations covers a more ample range than has been previously considered in related theoretical studies. It should be noted, however, that after relaxing the
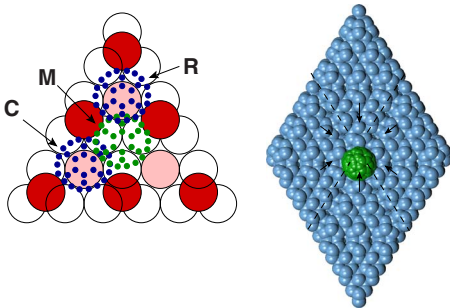

FIG. 3. (Color online) (Left) Schematic view of the C_{60} adsorption sites on the Si(111)7$\times$7 surface. (Right) C_{60} adsorbed at the corner hole (CH), displayed for clarity in a 2×2 supercell of the Si(111)7$\times$7 surface. The six adatoms whose dangling bonds are responsible for the chemisorption (see text) are indicated by the arrows.

TABLE I. Relative total energies, ΔE, and average C_{60} normal distance from the surface, $z(C_{60})$, for each adsorption configuration considered in this work. The values are given with respect to the most stable adsorption site found, namely, the CH. Fourth column contains the bond lengths between the fullerene and the Si surface atoms; superscript a and r stand for adatoms and rest atoms, respectively. Last column gives the average deviation of the Si atoms with respect to the clean p(7×7) case. The average for each configuration is taken over the five Si atoms which show larger deviations. All energies are in eV and distances are in Å.

	ΔE	$z(C_{60})$	d(C-Si)	$\|\delta r(Si)\|$
CH	0.00	0.0	1.9,2.0,2.1,2.1	0.4
C_U	0.05	0.8	$1.9, 1.9, 2.0, 2.0^a, 2.1^r, 2.1^r$	0.7
R_U	0.31	1.3	$1.9, 2.0^a, 2.0^r$	0.6
C_F	0.47	1.2	$2.0, 2.0, 2.0^a, 2.0^a, 2.0^r, 2.1^a$	0.8
M_F	0.94	1.2	$1.9, 2.0^a, 2.0^r$	0.6
R_F	1.31	1.9	2.0^r	0.2
M_U	2.81	2.9	2.2^a	0.2

system hybrid configurations could be obtained and distinguishing, for instance, a C from an M position could be sometimes ambiguous.

The most stable adsorption site that we have found is the CH. The relative stabilities of the other adsorption configurations are summarized in Table I, where we also provide details of the adsorption geometries such as the relative height of the C_{60}, the C-Si bond lengths and the displacements of the Si atoms with respect to the clean surface averaged over the five Si atoms which show largest deviations in each case. The values in the table reveal that the energy hierarchy results from a complex trade-off between the number of C-Si bonds and the substrate reconstruction.

At a first approximation, the reasons for the high stability of the C_{60} at the CH site can be understood by simple geometric arguments. The fullerene naturally fits in the corner hole and can achieve in principle a maximum coordination with the surface adatoms (see Fig. 3) with a minimal deformation of the substrate arrangement. The DFT relaxed geometry described in Table I reveals the formation of four C-Si bonds and moderate substrate relaxations.

When the fullerene is adsorbed in the proximity of the C positions, on the other hand, it undergoes a noticeable deformation which leads to a strongly bonded configuration comprising up to six carbon-adatom and carbon-rest-atom bonds. Such a bonding is possible because of the flexibility with which some carbon atoms of the C_{60} can partially rehybridize from sp^2 to sp^3 and bind one surface atom. As it is clearly seen in Fig. 4 and Table I, the adsorbed configuration is quite different from the minimal distortion of the corner hole. Here, both the fullerene and the surface atoms must readjust, finding a trade-off between elastic deformation and the formation of new bonds. We recall that such an *activity* of the surface dangling bonds was already observed in some of the tight-binding MD runs where the fullerene was adjusted until the most favorable configuration for the adsorption was met.

Remarkably, our C_U configuration, which is the most stable adsorption site besides the CH, has striking similarities
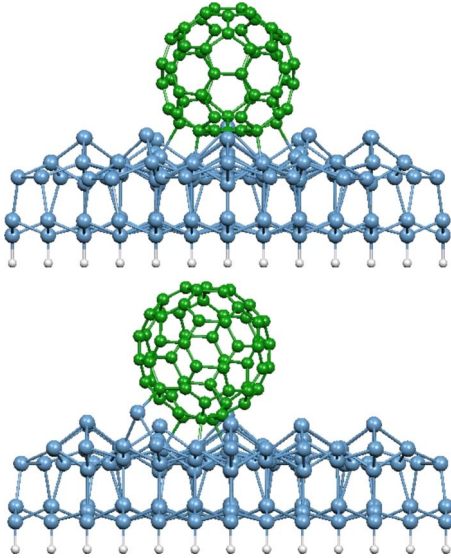
FIG. 4. (Color online) Adsorbed geometry of the C$_U$ (top panel) and C$_F$ configurations (bottom panel). Both the C$_{60}$ and the substrate undergo a relevant deformation in order to maximize the coordination with the surface dangling bonds.

FIG. 5. (Color online) Adsorbed geometry of the M$_U$ (top panel) and R$_F$ configurations (bottom panel). The orientation of the substrate is different from Fig. 4 for visual purposes.

with the *L configuration* that was found to be the most stable among those considered in Ref. 19. At this respect, it should be recalled that the CH could not be considered by Sánchez-Portal *et al.*[19] because they did not model the full Si(111)-p(7×7) surface and were restricted to a (2×2) adatom reconstruction.

The adsorption process and the adsorbed configurations when the C$_{60}$ is found close to the R and M positions shows qualitative differences with respect to the C positions. The R$_U$ and M$_F$ sites present a smaller coordination of 3 and the deformations of the fullerene and the surface are more moderate (see Table I). We have also found two weakly bound configurations, specifically positions R$_F$ and M$_U$, consisting of just one C-Si bond and a much larger molecule-substrate distance and where the fullerene and the surface are hardly distorted, pointing toward a hardly stable physisorbtion state (Fig. 5).

It is interesting to note that our TB-MD runs never ended with the fullerene at the CH position despite it being the most energetically favorable site. This result is in line with the experiments since the CH occupation is always considerably smaller than that at the F/UHs. This may be partly understood from kinetic arguments by recalling the large number of metastable configurations available at the F/UHs but also suggests that there is a considerable energy barrier associated to this highly symmetric site. This fact is indirectly confirmed by starting a MD run with the C$_{60}$ in the CH position. At least within the limited time span that can be covered by our simulations, the C$_{60}$ is found not to leave this high-symmetry position. On the other hand, if a C$_{60}$ is dropped on top of the CH position it is often adsorbed at neighboring local minima.

In order to understand the nature of the electronic interaction between the C$_{60}$ molecule and the silicon surface, we have calculated the PDOS on the molecular orbitals. Such an analysis delivers at the same time two very important pieces
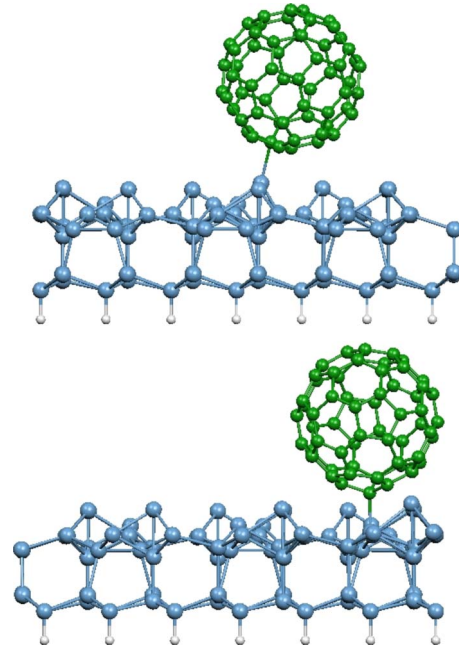
of information: (a) the degree of hybridization of the molecular orbitals with the substrate, i.e., strength of the interaction, by looking at the broadening and splitting of the peaks and (b) the charge transfer by observing how the molecular orbitals are located with respect to the Fermi energy of the system, i.e., if unoccupied MOs have been filled or occupied MOs have been emptied (charge transfer from the substrate to the molecule and vice versa, respectively).

We display in Fig. 6 the PDOS for all configurations computed from the self-consistent SIESTA Hamiltonian (left panel) and from the fitted EHT (right panel). The configurations have been ordered by decreasing adsorption energy from bottom to top. Solid dark lines compromise the HOMO, dashed dark the HOMO-1, solid gray the lowest unoccupied molecular orbital (LUMO), and dashed gray the LUMO+1 states of the isolated molecule. The agreement between the SIESTA and EHT derived PDOS is reasonable, with almost all peaks qualitatively reproduced. The larger discrepancy is found for the HOMO states, which appear at higher binding energies in the EHT case thus leading to larger molecular gaps. We ascribe this difference to the limited number of parameters varied in the PDOS fits (see Sec. II). Nevertheless, given the fact that DFT systematically underestimates the gap values, we do not find this fact relevant.

As we move from top to bottom in the graphs we find that the well-resolved peaks found for the less stable M$_U$ configuration gradually broaden as the interaction with the substrate increases. This is particularly evident for the LUMO states which rehybridize with the surface in a bonding antibonding fashion, a clear signature of covalent bonding, together with a considerable charge transfer coming from the occupation of the bondinglike states. For the weak-interaction limit, on the other hand, the bonding consists mainly of a charge-transfer process, revealed by the pinning around the Fermi level of
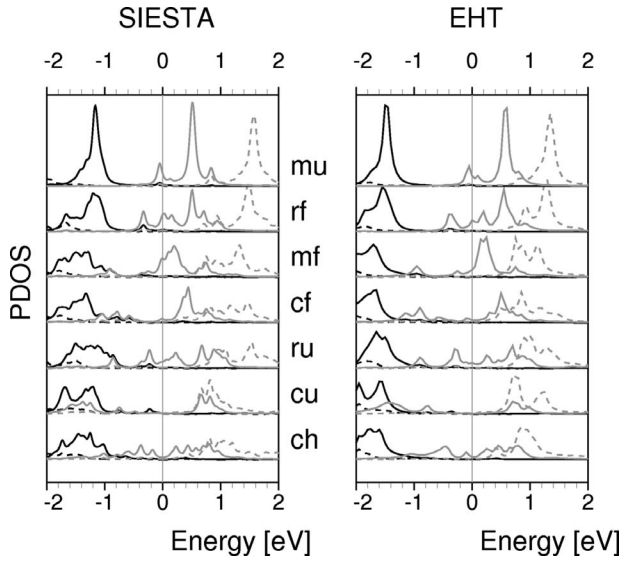
FIG. 6. DOS projected on to the C60s HOMO-1 (dark dashed), HOMO (dark solid), LUMO (gray solid), and LUMO+1 (gray dashed) for the seven C_{60} configurations studied in this work. Left and right panels correspond to the SIESTA-DFT and EHT-fitted results, respectively.

some of the LUMO orbitals. Another clear feature in the plots is the opening of the HOMO-LUMO+1 gap as ones move upwards in the figure. Summarizing, we find two limits in the adsorbed configurations: (a) a weak adsorption that relies on a charge transfer without the formation of new bonds and with no significant distortion of the molecule or restructuring of the surface (cases M_U or R_F in Fig. 6); (b) a strong adsorption where the fullerene undergoes a noticeable deformation in search of the highest possible coordination with adatoms and rest atoms of the substrate (cases CH, C_U, or R_U).

B. STM simulations

1. Clean Si(111)-p(7×7)

As a first test for the performance of our EHT-GREEN formalism, we present in Figs. 7(a) and 7(b) occupied and empty states topographic images simulated for the clean (7 ×7) surface employing the WSi tip. The simulations nicely reproduce the change in the aspect of the reconstruction with bias. In Fig. 7(c) we plot STS spectra calculated according to Eq. (3) with the electronically *frozen* Pt tip. We have averaged the STS signal placing the tip apex on top of the rest atoms (*R*) and on top of the adatoms (*A*). The so-called S_2, S'_1, and S_1 peaks are well resolved at energies −0.5, −0.35, and −0.1 eV, respectively, while the U_1, U'_1, and U''_1 peaks all show up as a single peak at around 0.2 eV denoted by U_1 in the figure. Deviations in the peak positions with respect to the RT experimental values[30] are at most 0.2 eV. Current image tunneling spectroscopy (CITS) maps are presented in Figs. 7(e) and 7(f) for the S_2, S_1, and U_1 states. Clearly, the first peak is associated to the rest atoms, the second to the corner adatoms while the third one combines contributions from all adatoms. Also notice the nonequivalence in the
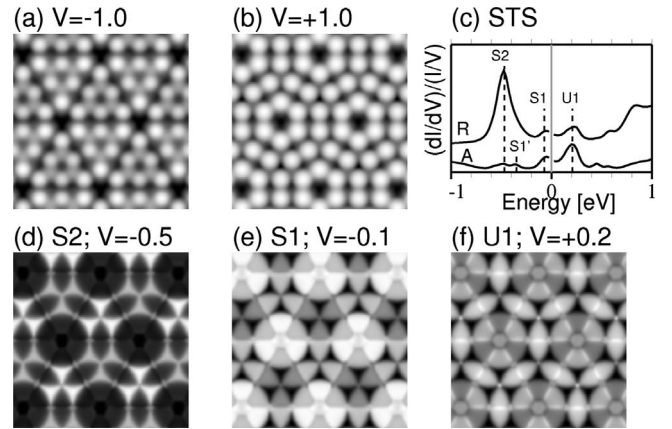

FIG. 7. (a) and (b) Simulated STM topography maps for the clean Si(111)-p(7×7) surface calculated with the WSi tip. Tunneling parameters are: $V=\pm 1.0$ V and $I=1$ nA. (c) STS spectra calculated on the p(7×7) surface employing the Pt tip. Top and bottom graphs are averages over the rest atoms (*r*) and adatoms (*a*), respectively. Peaks S_2, S'_1, S_1 and U are indicated by dashed lines. (d) and (f) CITS maps calculated with the Pt tip at selected energies so that the S_2, S_1, and U_1 states are clearly visible.

bright features between the faulted and unfaulted maps—in good qualitative agreement with the experimental results.[30]

2. Topography

We next address the STM simulations for the fullerene as a function of its adsorption geometry. Figure 8(a) shows (60×60) Å² topographic images simulated with the Pt tip and corresponding to the C_{60} adsorbed at the CH and M_U positions. The fullerene is imaged as a large bump with any intramolecular features hardly visible. In agreement with the images of Pascual *et al.*,[10] the weakly bound molecule M_U appears much brighter and larger than in the CH case, which
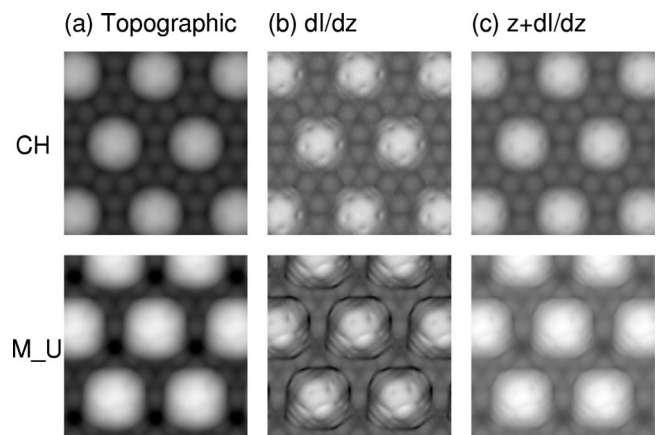

FIG. 8. Simulated STM maps for the C_{60} at the CH and M_U positions in different modes. (a) Topography using as set current I =1 nA, (b) dI/dz calculated with the tip height at each pixel set to the same value as in the topographic map and (c) the $z+dI/dz$ map obtained after summing up maps in (a) and 1.5 times (b). The same gray scale is used per column. All images computed for a bias of $V=-2$ eV.
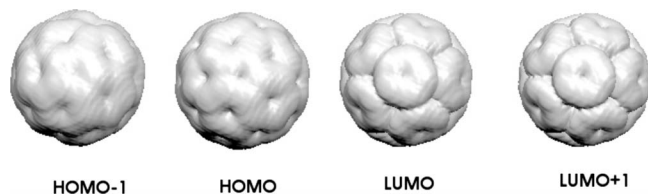
FIG. 9. LDOS contour surfaces for the C60s frontier molecular orbitals. The HOMO-1, HOMO, LUMO, and LUMO+1 are 4, 5, 3, and threefold degenerate, respectively.

is simply related to the fact that in the former geometry the C$_{60}$ is almost 3 Å higher from the surface. The molecule's apparent height for the rest of sites is always between these two limiting cases. On the other hand, Fig. 8(b) shows the corresponding derivative dI/dz maps, where a clear enhancement for the fullerene's internal structure is apparent and both the molecule and the surface adatoms can be resolved simultaneously. Since both types of imaging modes can be readily obtained in current experimental setups, we will show from now on the sum of both types of maps—the derivative term always premultiplied by 1.5—in order to view more clearly the molecule's internal structure. The result of this combined mode, denoted by $z+dI/dz$, is given in Fig. 8(c).

In order to aid the interpretation of the STM images presented below, LDOS isosurfaces for the C$_{60}$ MOs close to the Fermi level are displayed in Fig. 9. They have been calculated for the isolated nondistorted molecule, adding up the contribution of degenerate states; the degeneracies are 4, 5, 3, and 3 for the HOMO-1, HOMO, LUMO, and LUMO+1 states, respectively. We have checked that the LDOS surfaces hardly change if we consider instead the C$_{60}$ geometries found for each adsorption model despite the molecular distortions lift the degeneracies. The visual inspection of the LDOS reveals that the HOMO-1 and HOMO on one hand, and the LUMO and LUMO+1 on the other hand, are very similar. There are, however, marked differences between the occupied versus unoccupied LDOS and therefore, one would expect that STM images associated to empty and occupied states should differ considerably.

Figure 10 presents $z+dI/dz$ maps simulated with the Pt tip at different biases for some representative cases, namely:
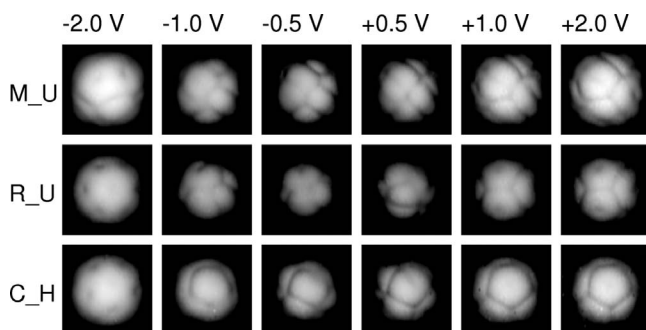

FIG. 10. Simulated STM $z+dI/dz$ maps for the CH, R$_U$, and M$_U$ adsorption geometries calculated with the Pt tip and for different biases. Size of images is $(20×20)$ Å^2. Tunneling parameters are: $V=\pm1.0$ V and $I=1$ nA.
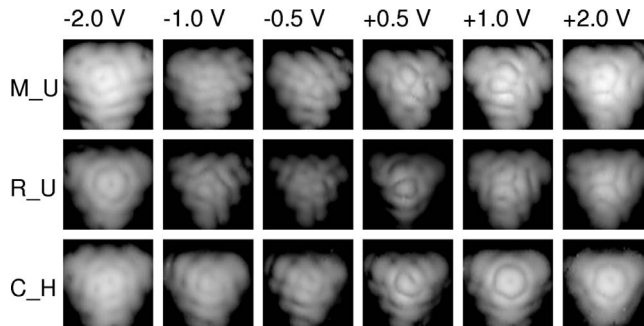

FIG. 11. Same as Fig. 10 but for the WSi tip.

CH, R$_U$ and M$_U$. The simulations for the other configurations show similar features but with different orientations. At large positive biases, (right column in Fig. 10) we find pentagons with different orientations but all of them reminiscent of the LUMO and/or LUMO+1 LDOS presented in Fig. 9. Recall, however, that the CH case does not show a dip at its center, while for the M$_U$ geometry we find a nodal line crossing the pentagon. At large negative biases, $V<-1.0$ V (left column in Fig. 10) the imaged fullerenes present a five-pointed star that resembles the HOMO and/or HOMO-1 LDOS displayed in Fig. 9. At intermediate biases, -1 V$\le V<+1$ V, we find a wide range of internal features which, in general, are different to those depicted in Fig. 9 and a direct correspondence with the C$_{60}$ MOs is not evident. Nevertheless, at these small voltages the fullerenes appear much dimmer since the tip apex comes closer to the molecule so that, from the experimental point view, the imaging process could become rather unstable.[13] Overall, our empty state STM images agree reasonably well with the available experimental data but, on the contrary, there are marked discrepancies for the occupied states case which we will further discuss in the next subsection.

We present in Fig. 11 equivalent $z+dI/dz$ maps for the same three adsorption geometries, but this time employing the WSi tip. The C$_{60}$ loses its rounded shape and now appears as large triangles, meaning that the fullerene is acting as a probe which scans the tip topography. The molecules apparent size is larger because the WSi tip is rather blunt. At large negative and positive biases one can still recognize at the center of the triangles similar features to those in Fig. 10, i.e., HOMO-1/HOMO and LUMO/LUMO+1 states, respectively. However, the sides of the triangles are now decorated by lots of extra strokes leading to an overall fullerene's aspect which differs substantially from those imaged with the clean Pt tip as well as from the LDOS in Fig. 9.

From the above comparison between the two tip results, we may conclude that the apparent shape of the fullerenes is strongly dependent on the tip topography and certain structural information on the tip could be directly extracted from it. This fact stresses the difficulty to experimentally view the C$_{60}$ frontier MOs in the topographic maps since these MOs may show up highly distorted due to their convolution with the tip apex atoms. Our results indicate that only images acquired with ideal–sharp and clean–tips can be interpreted in terms of the MO LDOS.
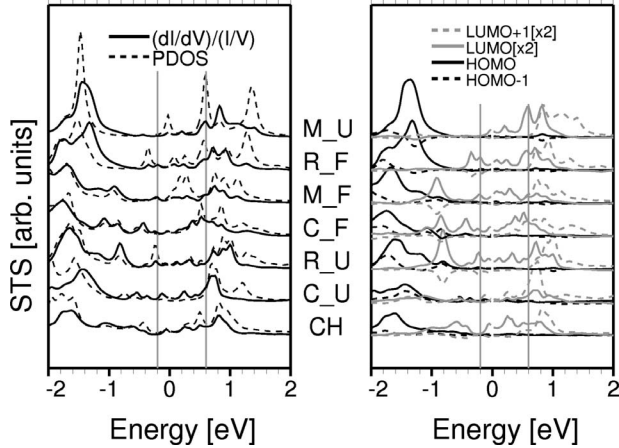
FIG. 12. Left panel: STS simulations for all the C_{60} adsorption geometries considered in this work, ordered from bottom to top in decreasing adsorption energy. Solid lines correspond to the normalized conductance, $(dI/dV)/(I/V)$, computed assuming an electronically flat tip, and averaged over 40–60 tip positions above the fullerene. Dashed line gives the DOS projected onto the C_{60} states. Right panel: the decomposition of the normalized conductance into contributions from the HOMO-1 (dashed black line), HOMO (solid black), LUMO (solid gray), and LUMO+1 (dashed gray) states for the same cases. For the sake of clarity, the latter two contributions have been magnified by a factor of 2. The theoretical Si bulk energy gap is indicated by the dashed vertical lines.

3. STS

Better insight into the nature of the states dictating the aspect of the fullerenes can be achieved by simulating STS data without taking into account the dependence of the tip's electronic structure with bias. To this end, we have applied Eq. (3) to all adsorption geometries using as set point in the $T(E)$ calculations the topographic map obtained at $V = +2.0$ V and $I = 1$ nA. We present in Fig. 12 the $(dI/dV)/(I/V)$ curves for all cases–solid lines in left panel, together with the corresponding DOS projected only onto the fullerene's states, dashed thin lines. In the right panel we present the decomposition of the $(dI/dV)/(I/V)$ curves in terms of the frontier MOs. Overall, the $(dI/dV)/(I/V)$ and PDOS spectra present the same peak structure, corroborating that the latter represents a good first approximation when interpreting the STS spectra. For biases larger than around $+0.7$ V the LUMO and LUMO+1 provide similar contributions and are responsible for the pentagonal structure seen in Fig. 10. This interpretation concurs with all previous works except for that of Pascual *et al.* At large negative biases the HOMO states (see Fig. 9) completely dominate the electron transmission and hence the five point star discernible in the images at the left in Fig. 10. Although these internal features were also found by Lee *et al.*,[12] they do not match the experimental images taken at negative voltages. This discrepancy was attributed to the DFT inaccuracy when predicting the energy location of the molecular levels. As suggested by Lee *et al.*, it is probable that the real HOMO states are located at larger binding energies, in which case one should

compare the experimental images with the theoretical ones calculated at smaller negative bias voltages. Inspecting Fig. 3 we find that in the region around the Fermi level only the LUMO states can be resolved. The associated STM images, displayed in Fig. 10, are again similar to those in Ref. 12 but still differ qualitatively from the experimental ones or those calculated by Hou *et al.* We cannot find a satisfactory explanation to this fact—our approach is more accurate—and probably more elaborate formalisms, e.g., self-consistent treatment of the electric field or an electronic description beyond standard DFT, will be necessary to elucidate this controversy.

A more detailed comparison between the normalized conductance and the PDOS reveals quantitative differences which could affect the interpretation of the STS data. First, in cases R_F and C_U there is a shift in the first HOMO related peak. Second, and more importantly, in most cases the relative height of the LUMO related peaks in the region $|V| < 1$ V are considerably smaller in the normalized conductance plots than in their PDOS counterparts so that these states may become almost invisible experimentally. This is particularly evident for the three less stable geometries: M_F, R_F, and M_U. A naive interpretation of their STS spectra would suggest that the two prominent features at around -1.5 and $+0.6$ eV are related to the HOMO and LUMO, respectively, thus leading to an erroneous molecular gap larger than 2 eV.

IV. CONCLUSIONS

We have studied the adsorption of C_{60} molecules on the $Si(111)7\times7$ surface with density-functional calculations. We have found the CH to be the most stable adsorption site, closely followed by the C_U site. Besides these strongly bonded configurations, characterized by covalent bonds between the C_{60} and the adatoms and rest atoms of the Si(111) surface, we have found weaker adsorption configurations where the interaction with the substrate consists mainly of a charge-transfer process and the C_{60} is virtually undistorted. Tight-binding molecular dynamics provide and interesting insight on how the surface adatoms select the best site and orientation for an efficient adsorption of the C_{60}.

Our STM/STS analysis brings two important conclusions. (i) The aspect of the fullerenes strongly depends on the tip nature and topography. In general, the tip contribution should be deconvoluted from the measured topographic images in order to extract direct information on the fullerene's electronic structure. (ii) At large positive voltages STM predominantly images the LUMO and LUMO+1 states while, unfortunately, at negative biases the interpretation of the images still needs to be fully understood.

ACKNOWLEDGMENTS

[1] Zhu Zhen-Ping and Gu Yong-Da, Carbon **34**, 173 (1996).

[2] O. Senftleben, T. Stimpel-Lindner, P. Iskra, J. Eisele, and H. Baumgärtner, Adv. Eng. Mater. **11**, 278 (2009).

[3] J. M. Ashcroft, D. A. Tsyboulski, K. B. Hartman, T. Y. Zakharian, J. W. Marks, R. B. Weisman, M. G. Rosenblum, and L. J. Wilson, Chem. Commun. (Cambridge) **2006**, 3004.

[4] J. Kröger, N. Néel, H. Jensen, R. Berndt, R. Rurali, and N. Lorente, J. Phys.: Condens. Matter **18**, S51 (2006).

[5] P. Moriarty, M. D. Upward, A. W. Dunn, Y.-R. Ma, P. H. Beton, and D. Teehan, Phys. Rev. B **57**, 362 (1998).

[6] G.-C. Liang and A. W. Ghosh, Phys. Rev. Lett. **95**, 076403 (2005).

[7] A. W. Dunn, E. D. Svensson, and C. Dekker, Surf. Sci. **498**, 237 (2002).

[8] C. Hobbs, L. Kantorovich, and J. D. Gale, Surf. Sci. **591**, 45 (2005).

[9] H. Wang, C. Zeng, Q. Li, B. Wang, J. Yang, J. G. Hou, and Q. Zhu, Surf. Sci. **442**, L1024 (1999).

[10] J. I. Pascual, J. Gómez-Herrero, C. Rogero, A. M. Baró, D. Sánchez-Portal, E. Artacho, P. Ordejón, and J. M. Soler, Chem. Phys. Lett. **321**, 78 (2000).

[11] C.-P. Huang, C.-C. Su, and M.-S. Ho, Appl. Surf. Sci. **254**, 7712 (2008).

[12] J. Y. Lee and M. H. Kang, Surf. Sci. **602**, 1408 (2008).

[13] J. G. Hou, Jinlong Yang, Haiqian Wang, Qunxiang Li, Changgan Zeng, Hai Lin, Wang Bing, D. M. Chen, and Qingshi Zhu, Phys. Rev. Lett. **83**, 3001 (1999).

[14] T. Thundat, R. J. Warmack, D. Ding, and R. N. Compton, Appl. Phys. Lett. **63**, 891 (1993).

[15] P. H. Beton, A. W. Dunn, and P. Moriarty, Appl. Phys. Lett. **67**, 1075 (1995).

[16] D. L. Keeling, M. J. Humphry, R. H. J. Fawcett, P. H. Beton, C. Hobbs, and L. Kantorovich, Phys. Rev. Lett. **94**, 146104 (2005).

[17] N. Martsinovich, C. Hobbs, L. Kantorovich, R. H. J. Fawcett, M. J. Humphry, D. L. Keeling, and P. H. Beton, Phys. Rev. B **74**, 085304 (2006).

[18] N. Martsinovich and L. Kantorovich, Nanotechnology **19**, 235702 (2008).

[19] D. Sánchez-Portal, E. Artacho, J. I. Pascual, J. Gómez-Herrero, R. M. Martin, and J. M. Soler, Surf. Sci. **482-485**, 39 (2001).

[20] J. M. Soler, E. Artacho, J. D. Gale, A. García, J. Junquera, P. Ordejón, and D. Sánchez-Portal, J. Phys.: Condens. Matter **14**, 2745 (2002).

[21] E. Artacho, D. Sánchez-Portal, P. Ordejón, A. García, and J. M. Soler, Phys. Status Solidi B **215**, 809 (1999).

[22] E. Anglada, J. M. Soler, J. Junquera, and E. Artacho, Phys. Rev. B **66**, 205101 (2002).

[23] D. Porezag, T. Frauenheim, T. Köhler, G. Seifert, and R. Kaschner, Phys. Rev. B **51**, 12947 (1995).

[24] R. Rurali and E. Hernández, Comput. Mater. Sci. **28**, 85 (2003).

[25] J. Cerdá, M. A. Van Hove, P. Sautet, and M. Salmeron, Phys. Rev. B **56**, 15885 (1997).

[26] B. Janta-Polczynski, J. I. Cerdá, G. Ethier-Majcher, K. Piyakis, and A. Rochefort, J. Appl. Phys. **104**, 023702 (2008).

[27] O. Paz, I. Brihuega, J. M. Gomez-Rodriguez, and J. M. Soler, Phys. Rev. Lett. **94**, 056103 (2005).

[28] J. Cerdá, A. Yoon, M. A. Van Hove, P. Sautet, M. Salmeron, and G. A. Somorjai, Phys. Rev. B **56**, 15900 (1997).

[29] J. Cerdá and F. Soria, Phys. Rev. B **61**, 7965 (2000).

[30] J. Mysliveček, A. Stróżecka, J. Steffl, P. Sobotík, I. Ošt'ádal, and B. Voigtländer, Phys. Rev. B **73**, 161302(R) (2006).